Research Square

Preprints are preliminary reports that have not undergone peer review.
They should not be considered conclusive, used to inform clinical practice,
or referenced by the media as validated information.

Fabrication of RGO@MnS/NC composite electrodes with stable and highrate capability for efficient sodium storage

Kun Wang
Gannan Normal universitiy
Ting Luo
Gannan Normal universitiy
Lei Liu
Gannan Normal universitiy
Wencong Wu
Gannan Normal universitiy
Shoujie Huang
Gannan Normal universitiy
Wenli Yao
Jiangxi University of Technology
Jirong Mou
Gannan Normal universitiy
Xiongdong Ma
Gannan Normal universitiy
Chao Zhang
Gannan Normal universitiy
Xiaokang Li
Gannan Normal universitiy
Jujun Yuan
yuanjujun@gnnu.edu.cn

Gannan Normal universitiy

Research Article

Keywords:

Posted Date: November 10th, 2026

DOI: https://doi.org/10.21203/rs.3.rs-11273731/v1

License: This work is licensed under a Creative Commons Attribution 4.0 International License.
Read Full License

Additional Declarations: No competing interests reported.

Fabrication of RGO@MnS/NC composite electrodes with stable and highrate capability for efficient sodium storage

[1]Kun Wang[1,2], Ting Luo[1,4], Lei Liu[1,2], Wencong Wu[1,2], Shoujie Huang[1,2], Wenli Yao[3,*], Jirong Mou[1], Xiangdong Ma[1], Chao Zhang[1], Xiaokang Li[1,4,*], Jujun Yuan[1,*]

[1]Future Energy Interdisciplinary Center, Key Laboratory of Solid-State Energy Conversion and Storage of Jiangxi Education Department, School of Intelligent Manufacturing and Future Energy, Gannan Normal University, Ganzhou, P. R. China

[2]School of Physics and Electronics, Gannan Normal University, Ganzhou, 341000, China

[3]Jiangxi Provincial Key laboratory of Power Battery & Energy Storage Materials, School of Materials Science and Engineering, Jiangxi University of Science and Technology, Ganzhou, 341000, China

[4]College of Chemistry and Materials, Gannan Normal University Ganzhou 341000, China

Abatract

MnS has drawn growing interest as an anode material for high-performance sodium-ion batteries, owing to its attractive theoretical capacity and favorable redox reversibility during the conversion-type reaction. Nevertheless, substantial volume expansion and sluggish reaction kinetics of MnS upon cycling processes trigger particle pulverization and rapid capacity fading. RGO@MnS/NC composites are fabricated through oxidative polymerization combined with carbothermal reduction–sulfurization. During the synthesis, MnS/NC nanoparticles are in situ immobilized on

* Corresponding author.

E-*mail Address:* lixiaokang@gnnu.edu.cn (X. Li); yaowenli@jxust.edu.cn (W Yao); yuanjujun@gnnu.edu.cn (J. Yuan);

conductive RGO nanosheets. When employed as an anode material for sodium-ion batteries (SIBs), the rationally engineered RGO@MnS/NC composites exhibit a stable reversible capacity of 140 mAh g^{-1} over 1200 long-term cycles under a high current density of 5 A g^{-1}. The outstanding cycling stability and rate capability of RGO@MnS/NC originate from its unique structural design. On one hand, MnS nanocrystals immobilized on RGO suppress particle agglomeration, expedite electron/ion transport, and facilitate adequate electrolyte penetration. On the other hand, the outer NC shell creates abundant active sites and further accelerates ion and electron transfer in the electrode. Benefiting from these advantages, RGO@MnS/NC composites hold great potential as a favorable anode material for advanced SIBs.

1. Introduction

Lithium-ion batteries (LIBs) are characterized by high voltage, high energy density, and long cycle life, and have thus been widely adopted in daily life[1, 2]. With the rapid deployment of LIBs in electric vehicles and large-scale smart grids, lithium is being increasingly consumed. However, lithium is constrained by its low crustal abundance, uneven geographical distribution, and persistently high market prices, limiting the further application of LIBs in large-scale energy storage. Sodium and lithium belong to the same main group and share similar physicochemical properties. Sodium resources are abundant in reserves, widely distributed, and low in cost, making sodium-ion batteries (SIBs) one of the promising candidates for next-generation large-scale energy storage[3, 4]. Owing to the relatively larger ionic radius of Na^+, electrode materials must possess sufficient sodium storage sites and efficient ion

transport pathways, thus precluding the direct adoption of those developed for LIBs. Therefore, exploring efficient anode materials and rationally optimizing performance regulation strategies is of great significance for the technological development of SIBs[5, 6].

Among the wide range of anode materials currently explored, transition metal sulfides have drawn extensive research interest owing to their remarkably high theoretical specific capacity, and are now recognized as one of the most promising candidate materials for SIB anodes[7, 8]. Of all the various transition metal sulfides, manganese-based sulfides have drawn particular attention for their low raw material cost, competitive theoretical capacity and high level of safety that make them an attractive option for battery anode applications[9-13]. However, manganese-based sulfides undergo obvious volume expansion during the electrochemical conversion with sodium ions, resulting in unsatisfactory cycling performance and rapid continuous capacity decay, which is normally caused by structural pulverization of electrode materials. To tackle the problems outlined above, research has demonstrated that manipulating the morphology of electrode materials and controlling their particle size can raise the specific surface area and enhance contact with the electrolyte[14, 15]. This approach effectively shortens the diffusion distance of alkali metal ions and speeds up their migration process. Meanwhile, when coupled with highly conductive carbon-based materials, it is able to mitigate volume swelling and boost the intrinsic electronic conductivity of the active material[16-22] For instance, MnS nanoparticles encapsulated into the amorphous N,S-codoped nanotube-like carbon (MnS@N,S-NTC) were syn-

thesized using MnO_2@PDA nanotube as template. The MnS@N,S-NTC electrode displayed 291 mAh g^{-1} at 250 mA g^{-1} after 200 cycles[16] . MnS nanocrystals embedded in carbon nanowires/RGO (MnS@CNWs/RGO) were fabricated via a facile strategy using manganese-coordination nanowires and GO as precursors. The MnS@CNWs/RGO electrode maintained an appreciable reversible capacity of 150 mAh/g at 1 A g^{-1} after 10000 cycles[18]. MnS@NC nanosheets were also produced through the topologic sulfurization of Mn(OH)(OCH_3)@PDA intermediate[19]. Attributed to its exceptional structure, the MnS@NC nanosheets exhibited a specific capacity of 189 mAh g^{-1} at 0.5 A g^{-1} after 200 cycles. As revealed by cycling results, targeted structural optimization effectively enhances the sodium storage capacity of MnS/C nanocomposites. Especially, two-dimensional configurations can suppress active material aggregation and breakage, facilitate charge migration and expand interfacial contact. Exploring novel two-dimensional MnS/C materials using convenient preparation strategies is therefore favorable for improving the anode performance of SIBs.

Herein, RGO@MnS/NC composites are synthesized via oxidative polymerization coupled with carbothermal reduction–sulfurization, where MnS/NC nanoparticles are in-situ anchored onto conductive RGO nanosheets. As an anode material for SIBs, the well-designed RGO@MnS/NC composites deliver a maintainable capacity of 140 mAh g^{-1} after 1200 long-term cycles at 5 A g^{-1}. The outstanding electrochemical property for RGO@MnS/NC composites can be attributed to their special hierarchical configuration, which simultaneously stabilizes electrode structures and accelerates the

transport of electrons and sodium ions.

2. Experimental

2.1 Fabrication of RGO@MnS/NC composites

The synthetic route of RGO@MnS/NC nanocomposites is illustrated in Fig. 1a. Firstly, 100 mg GO was dispersed in 100 mL deionized water and ultrasonicated for 20 min. Then, 0.13125 g dopamine hydrochloride (DA) and 0.5 mmol $MnCl_2 \cdot 4H_2O$ were added to the suspension, followed by 0.8325 g tris(hydroxymethyl)aminomethane (Tris). The mixture was magnetically stirred for 12 h, and GO nanosheet-supported Mn-PDA precursor was collected after centrifugation and drying. 100 mg GO@Mn-PDA precursor and 400 mg sulfur powder were uniformly ground, placed into a ceramic boat, and calcined in a tube furnace at 700 °C for 2 h under argon atmosphere to prepare MnS/NC nanosheet composites via carbothermal reduction-sulfurization.

2.2 Materials characterization

The crystalline phase and microscopic morphology of the RGO@MnS/NC composites were characterized by XRD (Panalytical Empyrean), FESEM ((Zeiss Gemini DSM 982), and TEM (JEOL JEM 3000 F). The content proportion of MnS in the RGO@MnS/NC hybrid was determined on a TGA (HENVEN HOT-4) setup under oxygen flow. The specific surface area of the RGO@MnS/NC sample was analyzed via a Quadrachrome Adsorption Instrument. The elemental composition of the RGO@MnS/NC material was examined with XPS (Axis Ultra DLD).

2.3 Electrochemical tests

Electrochemical tests on RGO@MnS/NC electrode materials were carried out in standard CR2032 coin cells, which were packaged inside an argon-sealed glove box. The working electrode was prepared via thorough blending of RGO@MnS/NC active substance, acetylene black and sodium alginate binder in the mass proportion of 7:2:1. Sodium metal foil served as the counter electrode, Cu foil was employed to form the conductive substrate, and glass fiber films were adopted as the separator. The electrolyte consisted of 1.0 M $NaClO_4$ dissolved in EC/DEC mixed solvent (1:1, volume ratio) containing 5 vol% FEC additive. Cyclic voltammetry (CV) and electrochemical impedance spectroscopy (EIS) tests were recorded on a VMP3 workstation. Galvanostatic charge-discharge cycling tests were collected with a Neware BTS-4000 battery testing system.

3. Result and discussion

The synthetic route to obtain RGO@MnS/NC composites is shown within Fig. 1a. To start with, the GO@Mn-PDA nanosheet precursor is synthesized via oxidative polymerization. During this process, dopamine molecules coordinate with dissociated Mn^{2+} cations and concurrently generate intermolecular interactions with GO sheets. Subsequently, the RGO@MnS/NC products were harvested after implementing carbothermal reduction and sulfurization on GO@Mn-PDA nanosheet precursorr at 700 ℃ over a 2-hour period under persistent argon atmosphere. Fig.1b-g presents the SEM images of GO@Mn-PDA nanosheet precursor and RGO@MnS/NC composites. As shown within Fig.1b-d, the precursor displays crumpled architectures assembled by OG nanosheets, with Mn-PDA tightly anchored onto the sheet surfaces. Fig. 1e and 1f

demonstrate that RGO@MnS/NC inherited the 3D nanosheet morphology of precursorMn-PDA@GO following carbothermal reduction/ sulfurization. High-magnification SEM observation (Fig. 1g) confirms that MnS nanoparticles are dispersedly immobilized on the surface of NC nanosheets.

The crystal structure of the RGO@MnS/NC composites was characterized using XRD analyzer. As shown in Fig. 2a, four characteristic diffraction signals located at 2θ=29.6°, 34.3°, 49.2°, and 61.3° correspond to the (111), (200), (220), and (222) crystal planes of cubic MnS according to the JCPDS card No. 06-0518. Moreover, a broad peak emerging at 20-25° is detectable, confirming the formation of RGO frameworks in the composite. Raman characterization of RGO@MnS/NC composites is presented in Fig. 2b, where representative D (~1353 cm^{-1}) and G (~1567 cm^{-1}) vibration peaks for disordered and graphitic carbon can be identified. The derived (I_D/I_G) of 1.26 reveals rich intrinsic defects in the carbonaceous matrix. As evidenced by BET characterization in Fig. 2c, the RGO@MnS/NC composites exhibit a high specific surface area of 65.57 $m^2\ g^{-1}$ and a pore size from 2.9 to 50 nm, verifying the generation of hierarchical porous frameworks. Fig. 2d presents thermogravimetric analysis (TGA) data intended to ascertain the MnS mass ratio contained in RGO@MnS/NC composites. Subjected to continuous heating between 25 °C and 800 °C in oxidizing gas, the sample suffered a total mass decline of 76.26%. Calculations built on the thermal oxidation chemical formula $3MnS+5O_2 \rightarrow Mn_3O_4+3SO_2\uparrow$ revealed that the MnS fraction of the composite reached 27.1 wt%.

TEM was used to characterize the microstructures of the RGO@MnS/NC com-

posites. TEM images displayed in Fig. 3a and 3b reveal that tens-of-nanometer MnS nanograins disperse evenly across RGO nanosheets. Moreover, NC outer layer originating from the PDA can be clearly distinguished at the periphery of these MnS nanoparticles. The HRTEM micrograph of the RGO@MnS/NC composites is provided in Fig. 3c. The interplanar distance measured to be 0.26 nm matches the characteristic (200) crystal facet of MnS. As shown in Fig. 3d, the HAADF TEM morphology coupled with its corresponding Mn, S, C, N EDX mapping patterns (Fig. 3d1-d4) of the RGO@MnS/NC sample offer extra evidence that MnS nanocrystals anchor uniformly on RGO nanosheets.

The elemental distribution and chemical bonding configurations of the RGO@MnS/NC composites were systematically investigated via XPS. The XPS survey scanning of the RGO@MnS/NC composites validated the presence of Mn, S, C and N elements within the synthesized material (Fig. S1).The Mn 2p XPS profile for the RGO@MnS/NC composites (Fig. 4a) presents two major photoelectron peaks at 641.78 eV and 653.28 eV, corresponding to Mn $2p_{3/2}$and Mn $2p_{1/2}$, alongside satellite features at 646.28 eV and 658.88 eV, which collectively confirm the characteristic signatures of Mn^{2+}[19]. The S 2p profile (Fig. 4b) displays four distinct characteristic peaks located at 161.78, 163.68, 164.88, and 168.08 eV, which are assigned to S-Mn , C-S-C, -C=S-, and SO_x bonds, respectively[22]. For the C 1s profile (Fig. 4c), four characteristic peaks centered at 284.78, 285.58 286.58, and 289.08 eV are attributed to C-C bonds, C=S bonds, C=O bonds, and N–C≡N bonds, respectively[22]. The N 1s profile (Fig. 4d) exhibits four characteristic peaks, which correspond to porphyrinic N

(397.88 eV), pyrrolic N (398.48 eV), and graphitic N (400.28 eV)[23].

CV together with galvanostatic charge-discharge measurements were adopted to investigate the sodium storage electrochemical characteristics of RGO@MnS/NC electrode. Fig. 5a presents the initial five cycles of CV profiles for the RGO@MnS/NC electrode collected at 0.1 mV s^{-1} within a voltage window of 0.01-3 V. In the first cathodic sweeping segment, the reduction peak close to 1.01 V stems from conversion reactions as well as irreversible electrolyte degradation for SEI film construction. The signal centered at roughly 0.04 V is attributed to the thorough reduction of MnS to Mn and Na_2S[17]. Within first anodic scan, the oxidation signals ranging from 1.56 V to 2.24 V correspond to the multistep oxidation process converting metallic Mn back into MnS[24]. Three continuous CV plots almost overlap each other from the third cycle, manifesting favorable reversibility and durable cycling behavior. Fig. 5b presents the galvanostatic charge-discharge curves of MnS/NC submicrospheres measured at a current density of 0.1 A g^{-1}. The material delivers initial discharge and charge specific capacities of 601 and 349 mAh g^{-1}, corresponding to a Coulombic efficiency of 58%. The decline in efficiency observed in the first cycle mainly originates from the irreversible generation of SEI films.

Fig. 5c displays the cyclic capacity property for the RGO@MnS/NC electrode at 0.1 A g^{-1}. After 100 cycles, the RGO@MnS/NC nanocomposite retains a reversible specific capacity of 259 mAh g^{-1}, which is considerably higher than that of the pure RGO electrode (157 mAh g^{-1}). Fig. 5d compares the rate capabilities of bare RGO and RGO@MnS/NC electrodes, revealing that the RGO@MnS/NC composites delivers

markedly enhanced rate performance. When the current density increases gradually from 0.1 to 5 A g^{-1}, the RGO@MnS/NC electrode delivers reversible specific capacities of 299, 274, 242, 211, 183, and 142 mAh g^{-1}, respectively. Notably, the reversible capacity recovers to 301 mAh g^{-1} when the current density is reset to 0.1 A g^{-1}. This phenomenon demonstrates that the RGO@MnS/NC electrode well preserves its structural integrity after repeated Na^+ insertion/extraction processes at high current densities, verifying its outstanding rate capability. The long-cycle stability for RGO@MnS/NC anode under high current densities is further investigated. At 1 A g^{-1}, the RGO@MnS/NC electrode maintains a reversible specific capacity of 210 mAh g^{-1} after 600 cycles (Fig. 5e), representing a capacity enhancement of 87.5% compared with the pure RGO electrode (112 mAh g^{-1}). Even at a high current density of 5 A g^{-1} (Fig. 5f), the RGO@MnS/NC electrode still achieves a reversible capacity of 140 mAh g^{-1} after 1200 cycles, which is more than twice that of the RGO electrode (58 mAh g^{-1}). These results comprehensively confirm that the RGO@MnS/NC electrode possesses superior long-term cyclic performance and structural stability，which can be comparable to those of previously reported MnS-based electrode materials (Table S1).

To investigate the electrochemical kinetic behaviors of RGO@MnS/NC composites, cyclic voltammetry tests were carried out at varied scanning rates ranging from 0.1 to 1 mV s^{-1}. As illustrated in Fig. 6a, all CV curves retain analogous contour features with distinct redox signals, whose peak intensities gradually rise along with elevated sweep speeds. The correlation between peak current (i) and scanning rate (v) follows the empirical formula $i=av^b$, where coefficient a stands for an inherent con-

stant of the electrode system and exponent b reflects the charge transport kinetic properties[25]. A calculated b value close to 0.5 points to a diffusion-controlled charge storage process, whereas a value approaching 1.0 corresponds to a capacitance-governed reaction pathway with rapid surface redox reactions[26]. Fig. 6b presents the fitted b parameters of four redox signals for the RGO@MnS/NC composites, which are 0.92 (peak 1), 0.98 (peak 2), and 0.86 (peak 3). These results confirm that the material is governed by dominant pseudocapacitive behaviors and fast charge transport. Via the current partitioning formula $i(V) = k_1v + k_2v^{1/2}$ capacitive contributions (k_1v) can be quantitatively decoupled from diffusion-controlled components ($k_2v^{1/2}$), enabling accurate quantification of their respective proportions in total charge accumulation[14]. Fig. 6c shows that the pseudocapacitance proportion of RGO@MnS/NC composites reaches 80.5% at a sweep speed of 1 mV s^{-1}. As displayed in Fig. 6d, the pseudocapacitive fraction of RGO@MnS/NC composites rises steadily from 61.0% to 82.4% when the scanning rate increases from 0.1 to 1 mV s^{-1}, which proves that surface-controlled charge storage pathways effectively boost the material's high-rate performance.

Electrochemical impedance spectroscopy (EIS) measurements were carried out following 5 and 20 charge-discharge cycles to quantify the Na^+ diffusion coefficient within MnS/NC submicron spheres. The EIS-derived Nyquist curve in Fig. 6e displays typical electrochemical signatures: an inclined linear segment at low frequencies associated with sodium ion diffusion, alongside a semicircular response across the medium and high frequency ranges that represents interfacial charge transfer re-

sistance[6]. The sodium ion apparent diffusion coefficient of RGO@MnS/NC composites can be derived by means of the impedance-based relation: $D_k^+=R^2T^2/2n^4F^4\sigma_w^2A^2C^2$, in which the real part of impedance varies with frequency according to the equation $Z'=R+\sigma_w w^{-1/2}$ (detailed derivation is provided in the ESI†). Electrochemical fitting results yielded Warburg factor (σ_w) values of 106.64 and 136.53 for RGO@MnS/NC composites after 5 and 20 cycles, respectively, as plotted in Fig. 6f. The corresponding sodium ion diffusion coefficients were calculated as 2.49×10^{-12} and 1.52×10^{-12}, which corroborates the outstanding sodium ion migration efficiency of the RGO@MnS/NC composites.The excellent cycling stability and rate capability of the RGO@MnS/NC composites originate from their peculiar structural architecture. On the one hand, MnS nanoparticles anchored on the RGO surface effectively inhibit particle aggregation, accelerate electron and ion diffusion behaviors, and guarantee sufficient electrolyte infiltration. On the other hand, the outer NC shell provides abundant reactive active sites and further promotes the transfer of ions and electrons within the electrode material.

4. Conclusion

In summary, the RGO@MnS/NC composites are successfully fabricated through a facile strategy combining oxidative polymerization with carbothermal reduction and sulfurization, in which MnS/NC nanoparticles were uniformly immobilized on conductive RGO nanosheets. When applied as an anode material for SIBs, the RGO@MnS/NC electrode delivers excellent rate performance and long-cycle durability. Specifically, it maintains a reversible specific capacity of 140 mAh g^{-1} even after

1200 cycles at a high current density of 5 A g^{-1}. The remarkable electrochemical superiority of the RGO@MnS/NC composites originates from its unique structural advantages. The immobilized MnS nanocrystals on the RGO substrate can efficiently suppress particle agglomeration, boost the migration of electrons and ions, and ensure adequate electrolyte penetration throughout the electrode. Meanwhile, the outer NC coating offers plentiful electrochemical active centers, further facilitating the rapid transfer of charge carriers and improving the overall electrochemical reaction kinetics.Therefore, this work provides a feasible strategy for the fabrication of high-performance RGO@MnS/NC anodes for sodium-ion batteries, which presents great potential for large-scale energy storage applications.

Author contributions

Kun Wang: resources, data curation, writing-original draft. Ting Luo: Data curation, Software. Lei Liu：Formal analysis. Wencong Wu：Writing-review & editing. Shoujie Huang: Investigation. Wenli Yao：Validation, Methodology. Jirong Mou: Investigation. Xiangdong Ma: Investigation. Chao Zhang: Formal analysis. Xiaokang Li: Validation, Methodology. Jujun Yuan: Writing-review & editing, Methodology.

Declaration of Competing Interest

There are no conflicts to declare.

Data availability

Data will be made available on request.

Acknowledgments

Natural Science Foundation of Jiangxi Province (20262BAC240302,

20253BAC280028, 20242BAB25230, 20262BAC240304), Key R&D Program of Science and Technology in Ganzhou (2023PCG16790), Gan Poyang Juncai Support Plan (20232BCJ25020), and Jiangxi Provincial High-Level Talent Project for Innovation and Entrepreneurship (xsq2023102011).

References

1. Z. Sun, Y. Liu, J. Chen, J. Liu, X. Zhou, F. Li, J. Zhao, M. Zhu, J. Liu, Unraveling degradation mechanism of electrolyte at high voltage and a hybridization strategy for non-flammable 4.8 V $LiCoO_2$ battery. Joule 9, 102166 (2025).

2. W. Liang, C. Li, S. Liu, Y. Li, H. Du, P. Zou, Y. Liu, Y. Zhu, H. Lin, K. Zhao, S. Zhou, C. Zhang, M. Lu, S. Bai, W. Wei, Z. Ma, J. Liu, Enabling high-voltage and wide-temperature quasi-solid-state batteries via spatially engineered polyether electrolyte interfaces. Joule 10, 102535 (2026).

3. R. Niu, D.R. Yang, J. Su, Y. Long, C. Li, Y. Jiang, X. Dai, X.W. Gao, Z.M. Liu, Q. Gu, X. Sun, W.B. Luo, From detrimental to functional: regulating residual alkalis as an interface resource on layer-structured transition-metal oxide cathodes. Adv. Funct. Mater. 36, e76483 (2026).

4. Z. He, Y. Huang, H. Liu, Z. Geng, Y. Li, S. Li, W. Deng, G. Zou, H. Hou, X. Ji, Anode materials for fast charging sodium-ion batteries. Nano Energy 129, 109996 (2024).

5. J. Yuan, X. Li, J. Liu, S. Zuo, X. Li, F. Li, Y. Gan, H. He, X. Xu, X. Zhang, J. Meng, Pomegranate-like structured Nb_2O_5/Carbon@N-doped carbon composites as ultrastable anode for advanced sodium/potassium-ion batteries. J. Colloid Interface Sci. 613, 84-93 (2022).

6. J. Yuan, Y. Gan, X. Xu, M. Mu, H. He, X. Li, X. Zhang, J. Liu, Construction of Fe_7Se_8@carbon nanotubes with enhanced sodium/potassium storage. J. Colloid Interface Sci. 626, 355-363 (2022).

7. Z. Yan, T. Sun, W. Li, Z. Long, R. Zhang, K. Wang, S. Wang, H. Qiao, Advances in metal sulfide anodes for high-performance sodium-ion batteries. CrystEngComm 27, 1225-1239 (2025).

8. A. Pramanik, S. Sengupta, S.K. Saju, S. Chattopadhyay, M. Kundu, P.M. Ajayan, Ternary metal

sulfides as electrode materials for Na/K-ion batteries and electrochemical supercapacitor: advances, challenges and prospects. Adv. Energy Mater. 14, 2401657 (2024).

9. S. Gao, G. Chen, Y. Dall'Agnese, Y. Wei, Z. Gao, Y. Gao, Flexible MnS–carbon fiber hybrids for lithium-ion and sodium-ion energy storage. Chem. Eur. J. 24, 13535-13539 (2018).

10. D. Cao, W. Fan, W. Kang, Y. Wang, K. Sun, J. Zhao, Z. Xiao, D. Sun, Metal−organic framework derived porous hollow ternary sulfide as robust anode material for sodium ion batteries. Mater. Today Energy 12, 53-61 (2019).

11. L. Wang, X. Tan, Q. Zhu, Z. Dong, X. Wu, K. Huang, J. Xu, The universality applications of MoS_2@MnS heterojunction hollow microspheres for univalence organic or multivalence aqueous electrolyte energy storage device. J. Power Sources 518, 230747 (2022).

12. H. Zhang, B. Liu, Z. Lu, J. Hu, J. Xie, A. Hao, Y. Cao, Sulfur-bridged bonds heightened Na-storage properties in MnS nanocubes encapsulated by S-doped carbon matrix synthesized via solvent-free tactics for high-performance hybrid sodium ion capacitors. Small 19, 2207214 (2023).

13. W. Liu, R. Huang, C. Yu, T. Xu, Y. Wang, H.Y. Yang, D. Yan, Y. Bai, Promoting robust and rapid Na-ion storage of molybdenum-based sulfide via rational hetero and hollow structure design. Small 35, 2500352 (2025).

14. J. Miao, N. Ci, B. Cao, G. Xie, X. Liu, H.J. Qiu, N, S-codoped 3D carbon protected nanoporous MnS with record high sodium ion storage performance for potential industry applications. Small 20, 2407829 (2024).

15. J. Yuan, X. Wang, M. Jing, H. Hu, M. Hu, Y. Bai, L. Yi, T. Wu, H. Hou, X. Wang, Ultrafine MnS/S-doped C composite prepared from Mn metal complex for sodium-ion battery with enhanced electrochemical kinetic behaviors. J. Energy Storage 137, 118722 (2025).

16. D.H. Liu, W.H. Li, Y.P. Zheng, Z. Cui, X. Yan, D.S. Liu, J. Wang, Y. Zhang, H.Y. Lü, F.Y. Bai, In situ encapsulating α-MnS into N,S-codoped nanotube-like carbon as advanced anode material: α→β phase transition promoted cycling stability and superior Li/Na-storage performance in half/full cells. Adv. Mater. 30, 1706317 (2018).

17. N. Zhang, X. Li, T. Hou, J. Guo, A. Fan, S. Jin, X. Sun, S. Cai, C. Zheng, MnS hollow microspheres combined with carbon nanotubes for enhanced performance sodium-ion battery anode. Chin. Chem. Lett. 31, 1221-1225 (2020).

18. Z. Sun, Y. Liu, D. Wu, K. Tan, L. Hou, C. Yuan, Construction of a multi-dimensional flexible MnS based paper electrode with ultra-stable and high-rate capability towards efficient sodium storage. Nanoscale 12, 4119-4127 (2020).

19. X. Chen, M. Zhang, Z. Liu, J. Cai, H. Fan, Y. Cui, Z. Wu, F. Peng, Synthesis of $Mn(OH)(OCH_3)$ as a novel precursor for 2D MnS-Based lithium- and sodium-ion battery anode materials. ChemElectroChem 9, e202200738 (2022).

20. J. Zhao, Y. Yang, C. Jiang, N. Ali Khan, X. Jia, H. Zhao, S. Ding, Ship in bottle synthesis of yolk-shell MnS@hollow carbon spheres for sodium storage. Nanotechnology 32, 505602 (2021).

21. D. Lan, Y. Zhao, Y. Liu, N. Zhu, J. Cui, Self-assembled nano-MnS@N,P dualdoped lignite based carbon as high-performance sodium-ion batteries anode. J. Energy Storage 90, 111827 (2024).

22. T. Luo, S. Lin, C. Zhang, X. Ma, Y. Li, X. Li, J. Mou, C. Wu, Z. Sun, J. Meng, J. Yuan, A facile synthetic strategy to MnS/NC submicrospheres for high-performance sodium-ion battery anodes. Mater. Res. Bull. 195, 113862 (2026).

23. J. Yuan, M. Mu, X. Xu, Y. Gan, H. He, X. Zhang, X. Li, F. Kuang, H. Li, J. Liu, Three-dimensional porous FeS@N doped carbon nanosheets for high-rate and high-stable sodium/potassium storage. Compos. Part B-Eng. 247, 110300 (2022).

24. C. Li, S. Liu, S. Lu, S. Wang, Q. Li, Y. Zhang, K. Cao, Construction of MnS nanocubes confined in N, S co-doped carbon as high-performance anodes for sodium-ion batteries. Inorg. Chem. Commun. 170, 113450 (2024).

25. Z. Song, G. Wang, Y. Chen, Q. Chang, Y. Lu, Z. Wen, Construction of hierarchical NiS@C/rGO heterostructures for enhanced sodium storage. Chem. Eng. J. 435, 134633 (2022).

26. S. Iqbal, L. Wang, Z. Kong, Y. Zhai, X. Sun, F. Wang, Z. Jing, X. He, J. Dou, L. Xu, In situ

growth of CoS_2/ZnS nanoparticles on graphene sheets as an ultralong cycling stability anode for potassium ion storage. ACS Appl. Mater. Interfaces 14, 15324-15336 (2022).

Fig. 1. (a) Schematic illustration of synthetic route for RGO@MnS/NC composites; (b-d) SEM images of GO@Mn-PDA nanosheet precursor; (e-g) SEM images of RGO@MnS/NC composites.

Fig. 2. (a) XRD pattern of RGO@MnS/NC composites; (b) Raman spectra of RGO@MnS/NC composites; (c) N_2 physisorption isotherms as well as pore size distribution curves obtained from RGO@MnS/NC composites; (d) TGA analysis of RGO@MnS/NC composites.

Fig. 3. (a,b) TEM images of RGO@MnS/NC composites; (c) HRTEM images of RGO@MnS/NC composites; (d) Corresponding EDX mapping of RGO@MnS/NC composites.

Fig. 4. XPS spectra of (a) Mn 2p, (b) S 2p, (c) C 1s and (d) N 1s for RGO@MnS/NC composites.

Fig. 5. (a) Cyclic voltammetry of RGO@MnS/NC composites at 0.1 mV s^{-1}; (b) Charge/discharge curves of RGO@MnS/NC composites at 0.1 A g^{-1}; (c) Cyclic capacity performance of RGO@MnS/NC composites at 0.1 A g^{-1}; (d) Rate behaviour of of RGO@MnS/NC composites; (e) Cyclic performance of RGO@MnS/NC composites at 1 A g^{-1}; (f) Cyclic performance of RGO@MnS/NC composites at 5 A g^{-1}.

Fig. 6. (a) Rate-dependent CV responses of RGO@MnS/NC composites; (b) The linear relationship between log (*i*) and log (scan rate) of RGO@MnS/NC composites; (c) Pseudocapacitive performance manifestation of RGO@MnS/NC composites in CV profiles at 1 mV s^{-1}; (d) Capacitive performance proportion at different sweep rates of RGO@MnS/NC composites; (e) EIS of RGO@MnS/NC composites; (f) Z' and $\omega^{-1/2}$ diagram of RGO@MnS/NC composites.

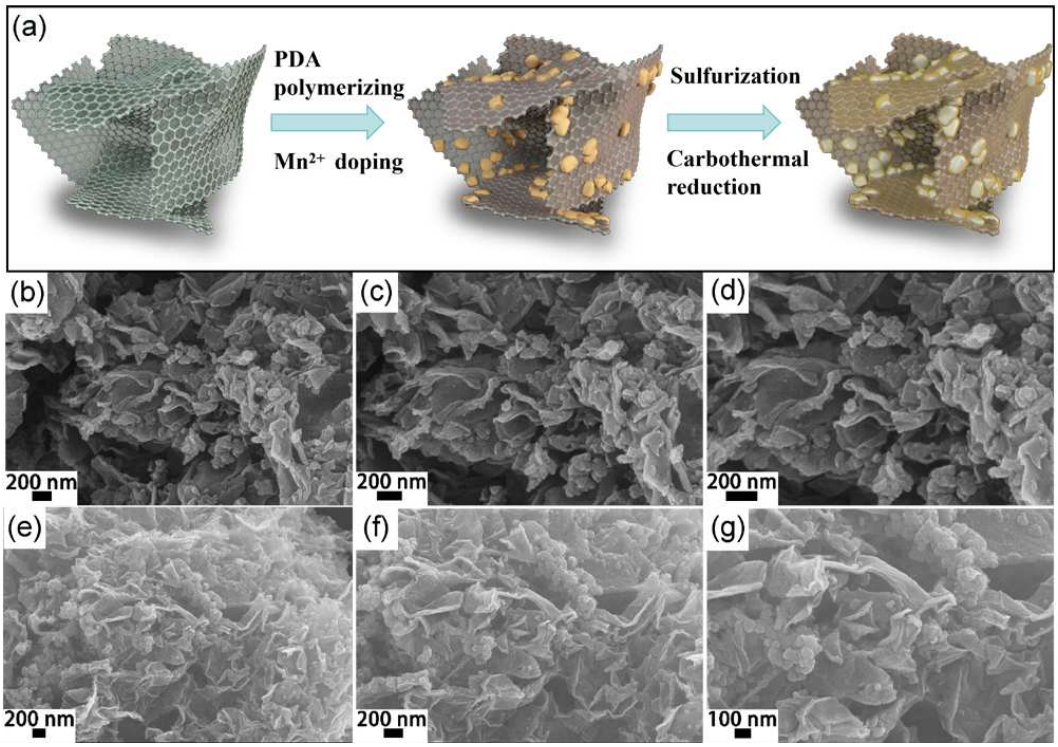

(a)
PDA
polymerizing
Mn2+ doping
Sulfurization
Carbothermal
reduction
(b)
(c)
(d)
200 nm
200 nm
200 nm
(e)
(f)
(g)
200 nm
200 nm
100 nm

Fig.1

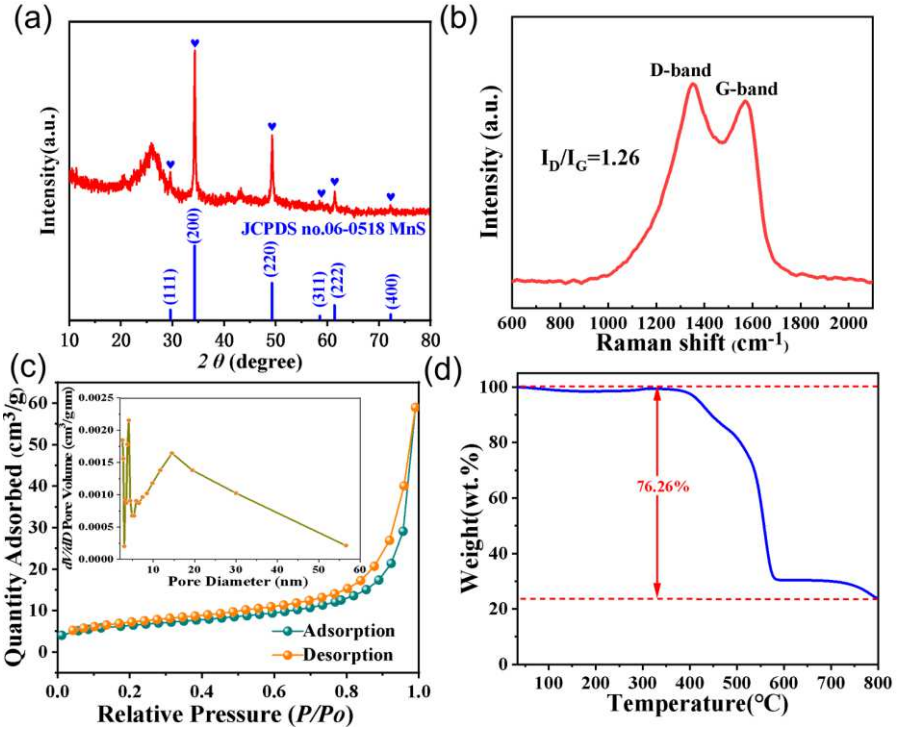

(a)
Intensity(a.u.)
JCPDS no.06-0518 MnS
(111)
(200)
(220)
(311)
(222)
(400)
2 θ (degree)
(b)
D-band
G-band
ID/IG=1.26
Intensity (a.u.)
Raman shift (cm-1)
(c)
Quantity Adsorbed (cm3/g)
dV/dD Pore Volume (cm3/g nm)
Pore Diameter (nm)
Adsorption
Desorption
Relative Pressure (P/Po)
(d)
76.26%
Weight(wt.%)
Temperature(℃)

Fig.2

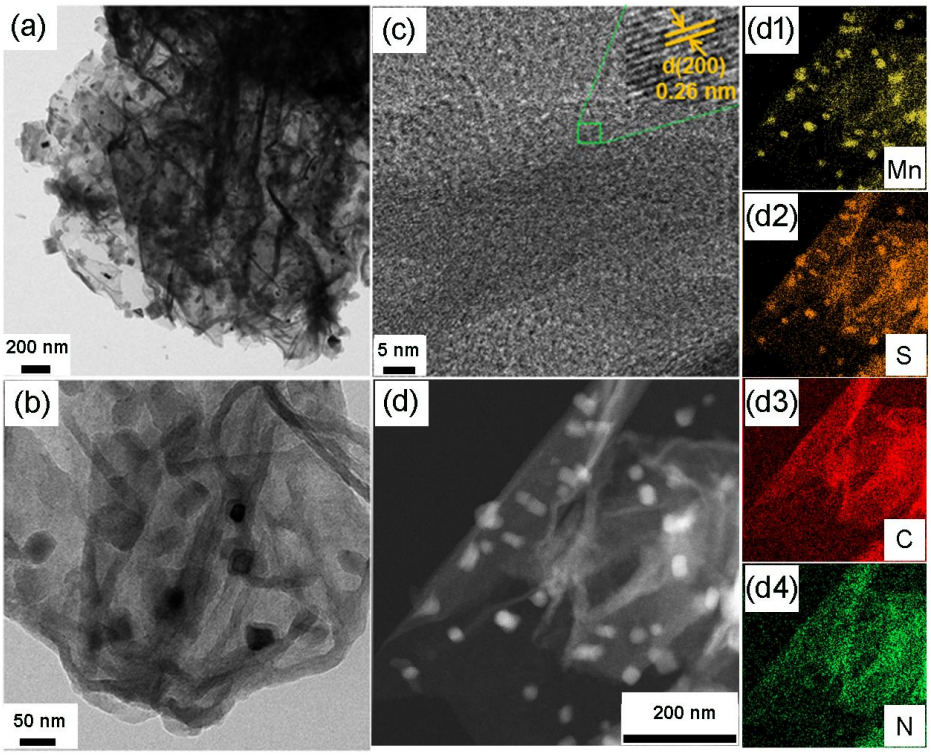

(a)
200 nm
(c)
d(200)
0.26 nm
5 nm
(d1)
Mn
(d2)
S
(b)
50 nm
(d)
200 nm
(d3)
C
(d4)
N

Fig.3

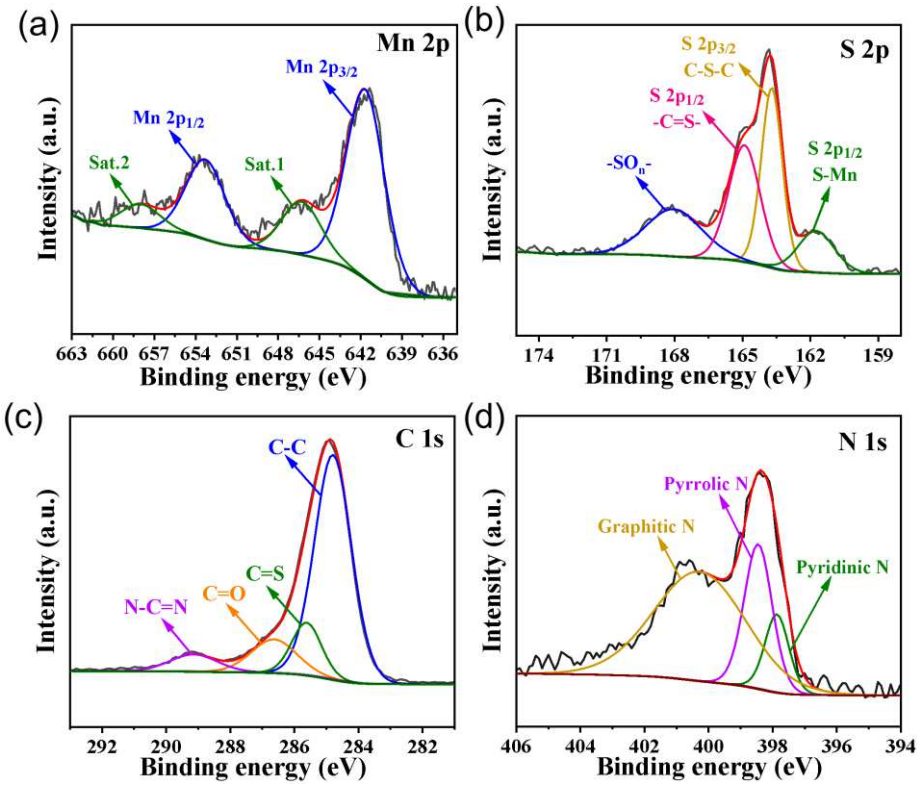

(a)
Mn 2p
Mn 2p3/2
Mn 2p1/2
Sat.2
Sat.1
Intensity (a.u.)
663 660 657 654 651 648 645 642 639 636
Binding energy (eV)
(b)
S 2p
S 2p3/2
C-S-C
S 2p1/2
-C=S-
-SOn-
S 2p1/2
S-Mn
Intensity (a.u.)
174 171 168 165 162 159
Binding energy (eV)
(c)
C 1s
C-C
C=S
C=O
N-C=N
Intensity (a.u.)
292 290 288 286 284 282
Binding energy (eV)
(d)
N 1s
Pyrrolic N
Graphitic N
Pyridinic N
Intensity (a.u.)
406 404 402 400 398 396 394
Binding energy (eV)

Fig.4

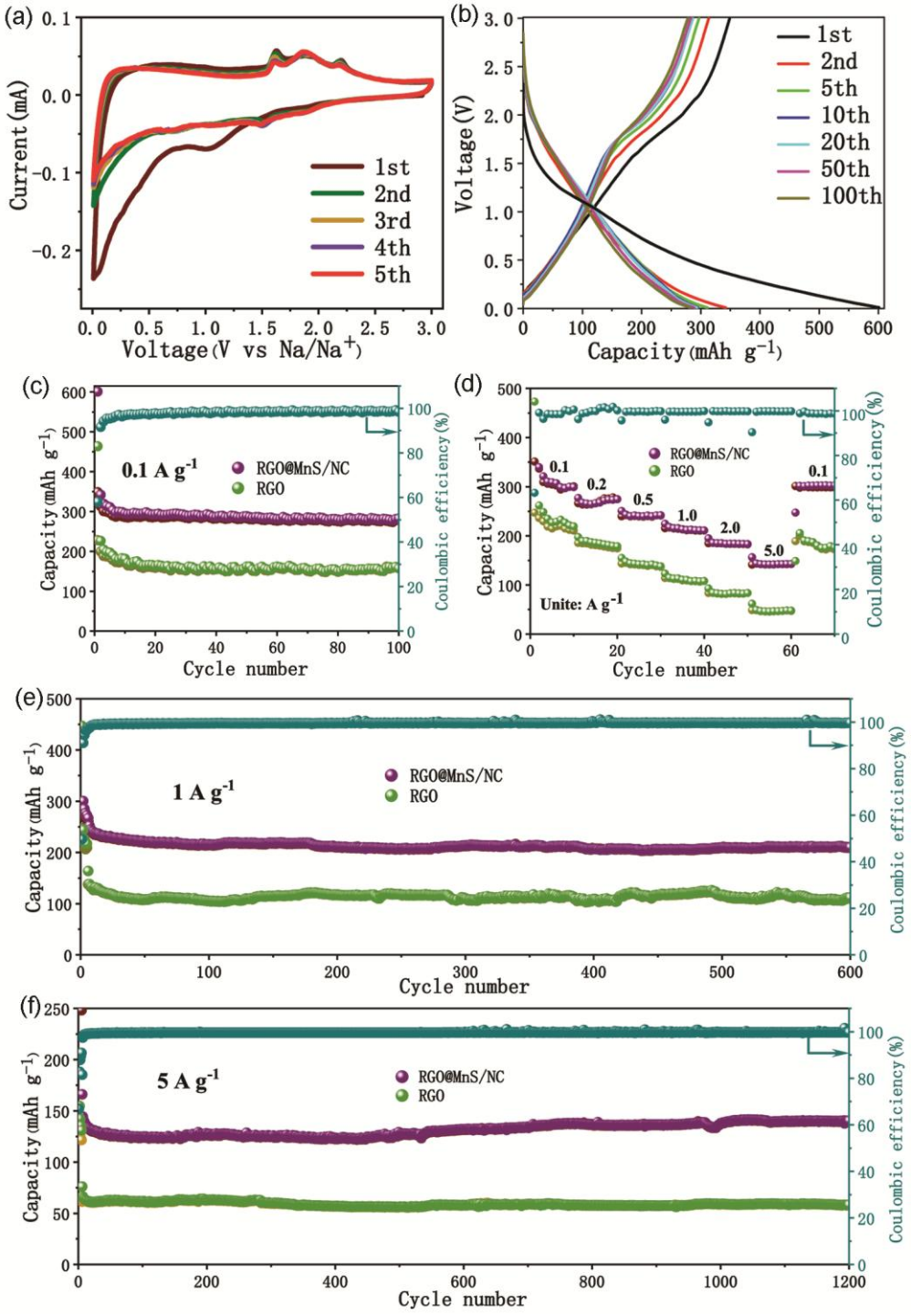

(a)
Current (mA)
Voltage (V vs Na/Na+)
1st
2nd
3rd
4th
5th
(b)
Voltage (V)
Capacity (mAh g-1)
1st
2nd
5th
10th
20th
50th
100th
(c)
0.1 A g-1
RGO@MnS/NC
RGO
Capacity (mAh g-1)
Coulombic efficiency (%)
Cycle number
(d)
RGO@MnS/NC
RGO
0.1
0.2
0.5
1.0
2.0
5.0
0.1
Unite: A g-1
Capacity (mAh g-1)
Coulombic efficiency (%)
Cycle number
(e)
1 A g-1
RGO@MnS/NC
RGO
Capacity (mAh g-1)
Coulombic efficiency (%)
Cycle number
(f)
5 A g-1
RGO@MnS/NC
RGO
Capacity (mAh g-1)
Coulombic efficiency (%)
Cycle number

Fig.5

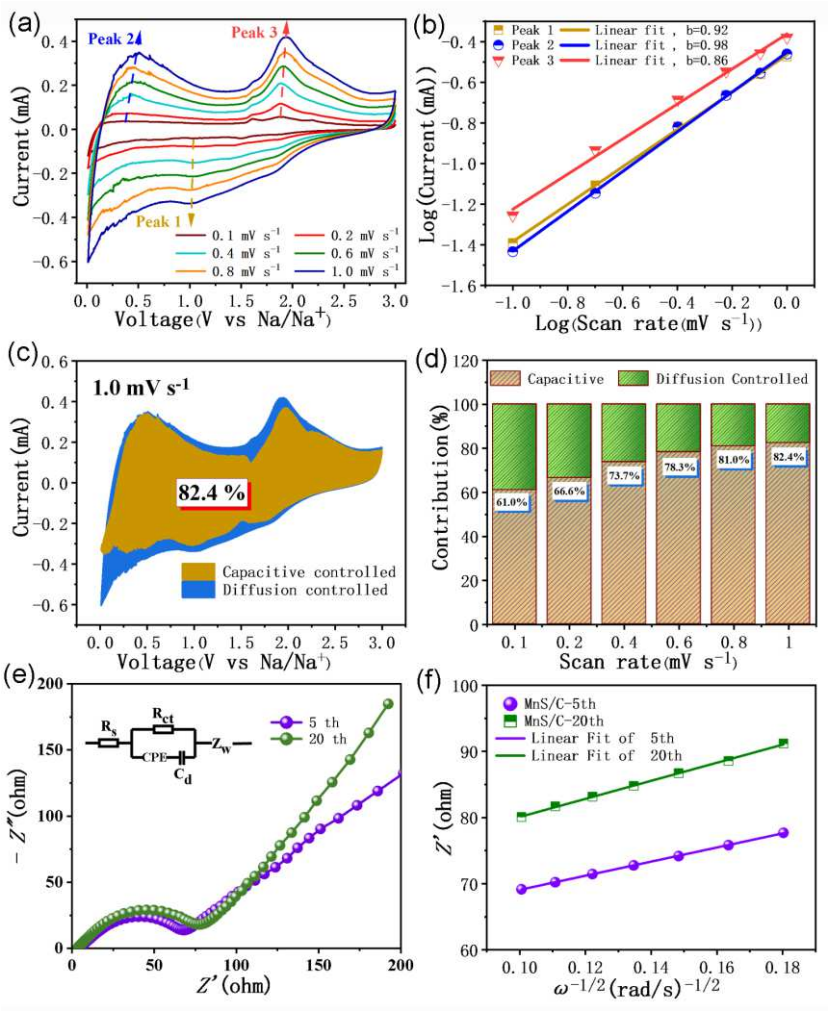

(a)
Peak 2
Peak 3
Peak 1
0.1 mV s⁻¹
0.2 mV s⁻¹
0.4 mV s⁻¹
0.6 mV s⁻¹
0.8 mV s⁻¹
1.0 mV s⁻¹
Current (mA)
Voltage (V vs Na/Na⁺)
(b)
Peak 1 Linear fit , b=0.92
Peak 2 Linear fit , b=0.98
Peak 3 Linear fit , b=0.86
Log (Current (mA))
Log (Scan rate (mV s⁻¹))
(c)
1.0 mV s⁻¹
82.4 %
Capacitive controlled
Diffusion controlled
Current (mA)
Voltage (V vs Na/Na⁺)
(d)
Capacitive
Diffusion Controlled
61.0%
66.6%
73.7%
78.3%
81.0%
82.4%
Contribution (%)
Scan rate (mV s⁻¹)
(e)
Rs
Rct
CPE
Zw
Cd
5 th
20 th
−Z″(ohm)
Z′(ohm)
(f)
MnS/C-5th
MnS/C-20th
Linear Fit of 5th
Linear Fit of 20th
Z′(ohm)
ω^−1/2 (rad/s)^−1/2

Fig.6

Supplementary Files

This is a list of supplementary files associated with this preprint. Click to download.

- JMSMESupportinginformation.docx